Sensors & Diagnostics

PAPER

View Article Online
View Journal | View Issue

Cite this: *Sens. Diagn.*, 2025, **4**, 538

Mode-directed photopatterning of whispering gallery mode optical resonators

Yuxiang Gao, [a] Vladislav Frenkel,[a] Stephen Arnold*[ab] and Rastislav Levicky*[a]

Multimodal optical resonators can integrate multiple sensing functions on a single device by assigning specific tasks to different modes. To facilitate such expanded functionality, this study demonstrates a photopatterning approach in which resonantly-amplified light within whispering gallery mode (WGM) sensors is used to direct chemical modification of the corresponding surface region addressed by the mode. A Ru(II) metallo–organic complex containing a caged aminopropyltriethoxysilane (APTES) moiety, [Ru(tpy)(biq)(APTES)]$(PF_6)_2$, was synthesized and applied as a covalently immobilized layer to solid supports to be patterned, including spheroidal silica WGM resonators. Exciting a mode caused the area exposed to the light to be deprotected, leaving behind a pattern of reactive amine groups available for further derivatization. A two-photon deprotection process enabled the use of near-IR sources for patterning. The photopatterning technique was applied to self-referenced measurements, in which signals from two modes, a sensing and a reference mode, were used to detect specific binding of avidin against a much larger background of nonspecific adsorption. This was accomplished by patterning the sensing mode with biotin to specifically bind avidin while the reference mode tracked nonspecific adsorption.

Received 19th January 2025,
Accepted 27th April 2025

DOI: 10.1039/d5sd00008d

rsc.li/sensors

Introduction

Patterning of molecules on surfaces is common in sensing applications.[1,2] On flat surfaces, patterning of binding ligands toward analytes of interest can be performed by printing of droplets[3–6] or through various writing,[1,7–9] photolithographic,[10,11] or stamp-based techniques.[12–14] However, for sensors with curved surfaces such as whispering gallery mode (WGM) optical microresonators, these conventional approaches become cumbersome to implement. WGM microresonators[15–19] come in curved geometries including ringlike, spheroidal, toroidal, cylindrical, and other shapes with radii of curvature in the tens of microns.[20,21] Similar to other optically resonant techniques,[22] WGM sensing is typically based on changes in refractive index.[23] Means for convenient patterning of WGM resonators would significantly expand their functionality; for example, in resonators supporting multiple modes, patterning individual modes could enable a single resonator to detect a multitude of analytes or to monitor nonspecific adsorption alongside specific signals.

WGM resonators trap light by circulating it under nearly total internal reflection,[24,25] allowing accumulation of the stored energy to intensities that far exceed that of the source. Tuning into the frequency of a specific resonant mode energizes the corresponding light pattern on the resonator surface. This selective light exposure, combined with suitable photochemistry, can in principle be used to direct immobilization of binding ligands or for other surface modification.

The present study demonstrates the concept of WGM photopatterning in spheroidal resonators. The spheroidal geometry supports many spectrally distinguishable modes, allowing individual modes to be independently energized and patterned. Because patterning is performed with the same modes as those used for detection, an additional benefit is that the generated pattern by default aligns with that subsequently needed for sensing.

One prospective application of resonators with patterned modes is self-referenced cancellation of nonspecific signals such as baseline drift. Compared to approaches that use separate resonators to monitor the specific and nonspecific signals,[26–31] combining both functions on a single device improves equivalence in local conditions, avoids geometrical or other mismatches between resonators, and simplifies overall system integration. In comparison with approaches based on linewidth sensing as a less drift-susceptible sensing modality,[32–36] self-referenced patterned resonators do not require analytes to be scattering or absorbing to markedly alter lifetime of the confined photons. Single-resonator self-referencing is perhaps closest to that realized by "splitting"

[a] *Department of Chemical & Biomolecular Engineering, New York University Tandon School of Engineering, Brooklyn, New York 11201, USA. E-mail: rl1306@nyu.edu*
[b] *Department of Applied Physics, New York University Tandon School of Engineering, Brooklyn, New York 11201, USA*

of energy-degenerate counterpropagating modes, which also uses just a single device.[19,37–40] However, because the modes of a spheroidal resonator are split from the outset by the geometry, in contrast to mode-splitting, the technique does not rely on heterogeneous deposition of analyte and is expected to be immune to buffer absorption losses that could obscure the mode-splitting.[41]

After describing preparation of the photoactive compound, based on a Ru complex with a caged aminoalkoxysilane, the compound is tested for photopatterning at near-IR wavelengths commonly used for WGM sensing. Patterning is observed at about half the energy of the complex's metal–ligand-charge-transfer (MLCT) band, and is attributed to uncaging of the silane by a two-photon mechanism. Next, a WGM resonator is configured for self-referenced sensing. In the self-referenced approach, one mode is patterned with a binding ligand and used to detect an analyte, while a nearby mode monitors baseline drift and nonspecific adsorption; the difference between the two signals is used to quantify specific binding. WGM photopatterning as demonstrated in this work adds to prior work based on use of multiple modes to expand diagnostic capabilities; *e.g.* for simultaneously locating and sizing analyte particles.[19,42]

Experimental

Materials

Unless indicated otherwise, all materials were from Millipore-Sigma and used as received, including $RuCl_3$ (hydrate); 2,2′:6′,2″-terpyridine (98%); 2,2′-biquinoline (98%); LiCl (99%); triethylamine (99.5%); $AgNO_3$ (99%); KPF_6 (99%); (3-aminopropyl)triethoxysilane (99%); sodium phosphate monobasic (dihydrate, 98%); sodium phosphate dibasic (99%); NHS-dPEG$_4$-biotin; avidin (egg white, 98%); methanol (99.9%); ethanol (anhydrous, 99.5%); acetone (99.5%); acetonitrile (99.5%); dichloromethane (99.8%); and 3 Å molecular sieves (beads, 4 to 8 mesh). Methanol was stored over molecular sieves to maintain a low water content. Activated neutral aluminum oxide for column chromatography was from HIMEDIA (Kennett Square, Pennsylvania), *N*-hydroxysuccinimide (NHS) esters of fluorescent dyes AF 488 and Cy5 were from Lumi Probe (Hunt Valley, Maryland), sulfuric acid (99.999%) was from Fisher Scientific (Ward Hill, Massachusetts), 50% hydrogen peroxide was from GFS Chemicals (Powell, Ohio), and dimethyl sulfoxide (DMSO, 99.9%) was from Nature's Gift (Ghent, Kentucky).

Synthesis of ruthenium complexes (Fig. 1)

1.) Ru(tpy)Cl$_3$ (ref. 43). 130 mg $RuCl_3 \cdot 3H_2O$ and one equivalent of 2,2′;6′,2″-terpyridine (tpy) were added to 15 ml of methanol. The mixture was heated to reflux and stirred for 4 hours, followed by cooling to room temperature and storage for 1 hr at −2 °C in a refrigerator. The brown solid was filtered and dried overnight under air. yield: 80%.

2.) [Ru(tpy)(biq)Cl]Cl (ref. 44). 200 mg Ru(tpy)Cl_3, 1 equivalent of 2,2′-biquinoline (biq), and 1 equivalent of LiCl were combined with 20 ml of a 1 : 3 water : ethanol solution. The mixture was deoxygenated for 10 minutes by nitrogen sparging, followed by addition of 1 ml of Et_3N. The solution was heated to reflux and stirred under a flowing N_2 blanket for 4 hours. The resultant mixture was filtered directly without cooling, and the filtrate was concentrated on a rotary evaporator until most of the liquid was removed. The remaining mixture was further dried overnight in a vacuum chamber. The recovered solid was purified over a neutral Al_2O_3 column by dissolving it in a 1 : 10 methanol : CH_2Cl_2 solution, and the first blue-purple band was collected. The solvent was again removed on a rotary evaporator and the remaining purple–black solid was dried in a vacuum chamber overnight. Yield: 85%.

3.) [Ru(tpy)(biq)(H$_2$O)](PF$_6$)$_2$ (ref. 44). 50 mg [Ru(tpy)(biq)Cl]Cl was dissolved in 9 ml of a 1 : 3 water : acetone solution and 3 equivalents of $AgNO_3$ solid were added. The mixture was deoxygenated with nitrogen gas for 10 minutes, and then refluxed while stirring under a flowing N_2 blanket for 7 hours. Next, the solution was cooled to room temperature and filtered to remove AgCl produced by the reaction. The filtrate was combined with 40 ml of saturated solution of KPF_6 in water, and the solution was cooled for 1 hour at −2 °C in a refrigerator. The formed purple–red solid was filtered and dried overnight under vacuum at room temperature. Yield: 60%.

4.) [Ru(tpy)(biq)(APTES)](PF$_6$)$_2$. 30 mg of [Ru(tpy)(biq)(H$_2$O)](PF$_6$)$_2$ was dissolved in 10 ml of absolute ethanol and the mixture was filtered to remove all insoluble solids. The solution was deoxygenated with N_2 for 10 minutes, heated to

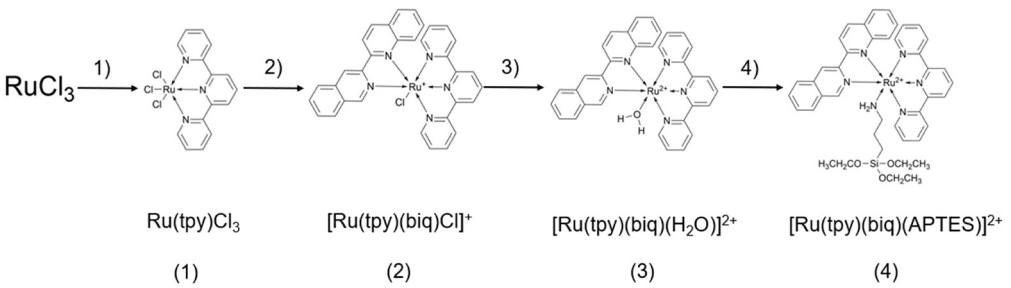

Fig. 1 Synthesis of [Ru(tpy)(biq)(APTES)](PF$_6$)^2.

reflux, and 40 μL of APTES was added and allowed to react for 6 hours while stirring under a flowing N_2 blanket. At the end of 6 hours, the solution was cooled to room temperature and purified on a C-18 reverse phase HPLC column with 100% methanol as the eluent to remove free APTES. The collected product, consisting of about a 1 : 1 mixture of compounds **3** and **4** coming off as two partly overlapping peaks, was collected and dried in a vacufuge. The dried product was stored in a freezer at −20 °C and in the dark until use, and could be safely used for up to three days. Yield: 50%.

Spectroscopic characterization

Absorbance spectroscopy was used to characterize intermediate Ru compounds on a Cary-50 spectrophotometer (Agilent Technologies; Santa Clara, California) from 200 to 700 nm at a 50 nm s^{-1} scan rate. A quartz microchannel cuvette was used to hold the test solutions.

Surface modification with [Ru(tpy)(biq)(APTES)]$(PF_6)_2$ (Ru-APTES)

Two types of solid supports were modified with Ru-APTES: soda-lime glass slides and amorphous silica WGM resonators. Resonators were fabricated by melting tips of optical fibers with a 10 W, 10 μm CO_2 laser (Synrad Inc; Mukilteo, Washington). A ZnSe lens and a reflector were used to focus the laser to a fine point on the fiber tip, causing it to melt and bead into a nearly spherical drop. The size of the drop was monitored by a microscope with a camera so as to arrive at a final radius of around 50 μm. *Caution: CO_2 lasers produce invisible beams capable of causing immediate burns to tissue. Appropriate personal protective equipment and access barriers are required to minimize health risks during operation*.

Prior to deposition of Ru-APTES, supports were cleaned with an air plasma (Harrick Plasma; Ithaca, New York) under a pressure of 0.1 mbar for 20 minutes, followed by immersion in 90 °C "piranha solution" (7 : 3 solution of 98% H_2SO_4 to 50% H_2O_2) for 20 minutes. *Caution: Piranha solution is extremely corrosive and suitable personal protective equipment must be worn during its handling. Because of gas evolution, piranha solution and its waste must be stored in vented containers*. Lastly, supports were extensively washed with deionized (DI) water and stored in acetone for up to 10 minutes before use.

Ru-APTES films were prepared by dissolving HPLC-purified Ru(II)-APTES in acetone to prepare a 50 μmol L^{-1}, purple-red solution. As stated earlier, these solutions contained significant amounts of the precursor Ru(II)-H_2O compound **3**; however, only compound **4** had the APTES moiety required for immobilization. Cleaned supports were immersed in the Ru-APTES solution for 6 hours at room temperature. After 6 hours, Ru-APTES modified supports were washed with a 1 : 1 acetone : water solution to remove unattached silane, followed by curing under partial vacuum (0.02 MPa) at 90 °C for 1 hour to crosslink the film. Cured films were sonicated in water for 10 seconds to remove any remaining unattached material, and immediately used for experiments.

Photopatterning

Initial tests to pattern Ru-APTES films on glass slides, based on a one photon process, used a 532 nm green laser with a 30 mW output. DI water was used to cover a region of the slide while an approximately 1.5 mm diameter spot was irradiated, corresponding to a patterning intensity on the order of 1 W cm^{-2}. DI water is intended to assist with displacement of APTES by H_2O as Ru groups are removed. After 30 minutes of irradiation, the glass slide was washed with DI water and immersed in a 30 μM solution of Cy5 NHS-ester in DMSO for 30 minutes. The slide was then washed with DMSO followed by DI water, dried, and the created pattern was imaged in a total internal reflection fluorescence (TIRF) geometry using a TIRF stage (TIRF Technologies; Morrisville, North Carolina) mounted on a Nikon Diaphot inverted microscope equipped with a 532 nm, 0.35 W laser (Laserglow; Clifton, New Jersey) and an Andor iXon Ultra (Belfast, Northern Ireland) camera. Photopatterning of spheroidal WGM resonators, based on a two photon process, was performed using a 1064 nm, 0.5 mW distributed feedback (DFB) laser module on a Mark I (MP3 Laser Inc, Burlington, Massachusetts) WGM workstation. Resonators were coupled to a tapered fiber waveguide inside a solution sample cell.[45] All WGM experiments were performed with polarization parallel to the silica surface, thereby exciting transverse electric (TE) modes. The scan range was restricted to the resonant mode to be patterned, which was repeatedly scanned over for 30 minutes. Wider spectra to determine the position and lineshape of the mode and neighboring modes were also captured at the start and end of this period. The effective power used for patterning depends on amplification provided by the resonator, which is about three decades for resonators used in this study. About a tenth of that is distributed over the evanescently-illuminated surface areas, which themselves cover approximately 10^{-5} cm^2 per mode; this translates to effective intensities of 10^3 to 10^4 W cm^{-2} used for two-photon, near-IR patterning. Afterwards, the resonator was washed with water and immersed for 30 minutes in a 13 μM solution of AF-488 NHS-ester in DMSO. The resonators were then washed by DI water and the AF-488 fluorescence distribution was imaged on a Leica TSC SP8 X confocal microscope (Deerfield, Illinois). Excitation wavelength was set at 488 nm, with emission filtered from 505 to 540 nm. The focus plane was adjusted to scan vertically at approximately 3 μm increments, depending on size of the resonator. For each image, resolution was set to 1024 × 1024, covering an area of 291 μm × 291 μm, with scan speed set at 200 Hz.

Self-referenced sensing

One mode, denoted as the "sensing" channel, was patterned with biotin while a second, unpatterned mode, served as a

"reference" channel. Ru-APTES modification and two-photon deprotection of the sensing mode were carried out as described earlier. Following the photodeprotection step to generate free amine groups, 30 volume equivalents of a 0.01 M, pH 7.3 sodium phosphate buffer (SPB) were injected into the WGM cell to wash the resonator. Next, six cell volume equivalents of 20 μmol L^{-1} biotin-d$(PEG)_4$ NHS ester in SPB were injected over one minute, followed by a 20-minute wait, after which the resonator was again washed with 30 equivalents of SPB buffer. Lastly, to perform the binding assay, four cell volume equivalents of a 500 nM solution of avidin in SPB were injected over 1.5 minutes and left in the cell. Shifts in the spectral positions of the sensing and reference resonances were monitored as a function of time. Self-referenced binding curves were calculated as the difference between the sensing and reference signals.

Results & discussion

A particularly suitable light source for WGM applications are near-IR distributed feedback (DFB) lasers,[46–48] favoured due to their MHz level resolution, spectral tunability, and affordability. These same sources would ideally be used for photopatterning of WGM resonators, provided a compatible photochemistry can be identified. One such class of compounds, with near-IR photoactivity based on a two photon mechanism, are ruthenium polypyridyl complexes.[49–52] These complexes are typically photoactive from 500 to 600 nm, or at twice those wavelengths for a two photon response,[51,52] in principle providing compatibility with common DFB laser sources operating at around 1 μm. In these compounds the Ru complex can act as a protecting cap on an amine coordinating to the Ru center; if the amine is part of an aminoalkoxysilane, the silane moiety can facilitate immobilization of the complex to silanol presenting surfaces.[51,53,54] Once immobilized, the free amine can be regenerated by photocleaving off the Ru cap and then used to direct further functionalization of the surface.

The compound selected for the present study, [Ru(tpy)(biq)(APTES)]$(PF_6)_2$ (Ru-APTES, Fig. 1), incorporates (3-aminopropyl)triethoxysilane (APTES) as the aminoalkoxysilane, which can be uncaged through a metal–ligand-charge-transfer (MLCT) oxidation process.[55,56] The position of the MLCT band depends on ligands surrounding the Ru center and can be used to monitor the stepwise preparation of Ru-APTES. Fig. 2 shows spectra for compounds (**2**) through (**4**), where the exchangeable monodentate ligand varies from Cl to H_2O to APTES. Among the three complexes, the Cl^- form exhibits the highest electron-donating character, while H_2O has the strongest electron-accepting character, with APTES in between. Accordingly, the maximum of the MLCT band shifts to longer wavelengths proceeding from compound (**3**) to compound (**4**) to (**2**), in agreement with the electron donating character of the ligand. Electron donors, such as Cl^-, enhance the electron density at the Ru(II) center, facilitating the MLCT process and resulting in a longer wavelength for the MLCT band. In contrast, electron acceptors induce a shift towards shorter wavelengths. These spectra also show that the optimal wavelength for one-photon deprotection should be around 560 nm, and around 1120 nm for a two-photon mechanism.

Initial photopatterning tests were performed using Ru-APTES modified soda-lime glass slides and a one-photon process. The slide was covered with deionized water and irradiated with a 30 mW, 532 nm laser. Afterward the slide was immersed in a solution of Cy5 NHS-ester in DMSO with the expectation that the fluorophore would immobilize wherever there were deprotected amines, followed by imaging with TIRF microscopy. As seen in Fig. 3, the region exposed to the laser was modified with the fluorophore, while surrounding areas that were not irradiated remained unmodified. These results confirmed that Ru-APTES films support one-photon deprotection and that the deprotected regions support further modification and patterning.

Compared to one-photon deprotection in the visible range, demonstrating a two-photon process in the near-IR is more challenging. Two-photon processes have lower absorption

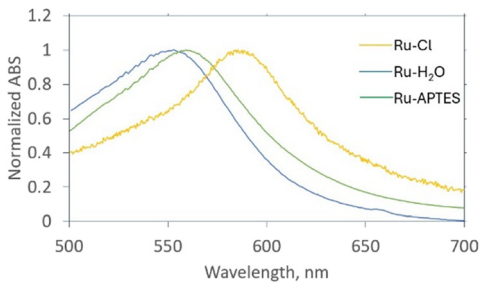

Fig. 2 Spectra of the MLCT region for Ru–Cl (compound **2**), Ru-H_2O (compound **3**), and Ru-APTES (compound **4**).

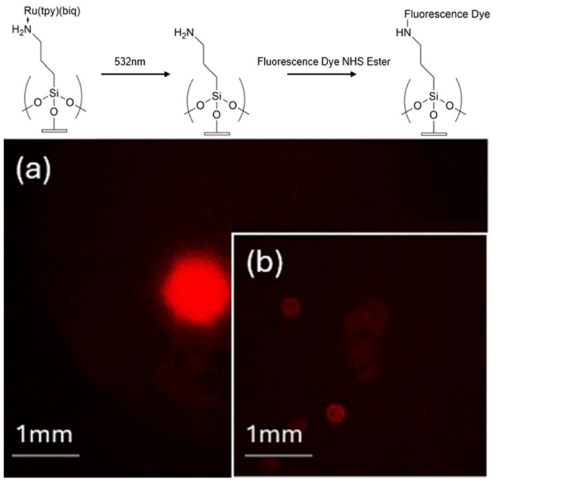

Fig. 3 Fluorescence image of a slide that was modified with Ru-APTES, irradiated with a 30 mW, 532 nm laser for (a) 30 min or (b) 0 min, followed by reaction with Cy5-NHS. Immobilization of the dye was observed only within the irradiated area.

cross sections as well as a second order dependence on light intensity:[57–59] overcoming these limitations is expected to require higher intensity sources. One alternative is to make use of the resonant amplification provided by the WGM mechanism, which can increase the modest power outputs of typical near-IR DFB lasers by several orders of magnitude. The amplification results from trapping light, coupled in from a waveguide, under nearly total internal reflection around a closed path;[17] constructive interference requires that the pathlength corresponds to an integer number of wavelengths. For a spherical resonator, this requirement leads to $l\lambda_0 = 2\pi R n_{\text{eff}}$ where R is the resonator radius, n_{eff} is an effective refractive index experienced by the trapped light that depends on its polarization as well as optical properties of the resonator and host medium, λ_0 is the wavelength in vacuum, and l is the integer number of wavelengths.

The spheroidal, slightly prolate resonators used in this study support hundreds of resonant modes that differ in tilt from the resonator's equator.[60–62] The modal intensity distributions at steady state can be visualized as comprised of one or more parallel rings of varying intensity, Fig. 4. The simplest resonant mode is the "equatorial" mode which consists of a single circular band around the midsection of the resonator. For purposes of discussion the modes can be indexed by l, the number of wavelengths around the resonator, which relates to the total angular momentum of the trapped photons, and m, which relates to the tilt of a mode, with $m = l$ for the equatorial mode and with the tilt relative to equator increasing as m decreases (m can also be considered to measure the z-axis projection of angular momentum, with $m/l = \cos(\theta)$ where θ is measured from the z-axis).[45] Amplification depends on how many times on average a trapped photon circulates before it is lost by scattering or absorption; the number of orbits can be determined from the resonance linewidth and is on the order of 10^3 for conditions of this study.

In principle, any of the hundreds of modes could be used for patterning. In a prolate resonator, the shortest resonant wavelength is observed for the equatorial $m = l$ mode, and increases as m decreases because the orbit perimeter increases with tilt. The resultant spectral separation between modes allows their individual addressing by tuning the laser to the corresponding wavelength, enabling the modes to be individually energized for patterning.

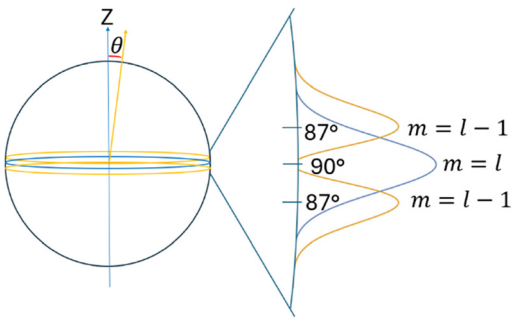

Fig. 4 Location of the equatorial mode (blue) and its neighboring mode (yellow) on the resonator. The expanded view at right shows the corresponding intensity profiles. The equatorial mode consists of a single band of intensity centered at $\theta = 90°$.

The equatorial mode, which concentrates its intensity into a single, uniformly energized band (Fig. 4), was chosen for testing two-photon patterning. The equatorial mode also avoids nonuniform illumination that could arise due to modal precession associated with "tilted" (*i.e.* $m \neq l$) modes.[61,63] After modifying the resonator with Ru-APTES, a 1064 nm DFB laser was repeatedly scanned across the equatorial resonance for 30 minutes. A wider scan, Fig. 5a, was also performed at the start and end to determine lineshapes of the equatorial as well as the nearest untreated mode. Fig. 5b and c present zoomed in overlays of the "before" and "after" scans for these modes. For the irradiated equatorial mode, Fig. 5b, the treatment sharpened the resonance. In comparison, the untreated $m = l - 1$ mode was unaffected, Fig. 5c. These observations are consistent with the expected, spatially selective uncaging of APTES on the equatorial mode. Since the Ru complexes absorb at these wavelengths, when present they shorten the average photon lifetime, resulting in a broader lineshape. Conversely, when there are fewer of the complexes remaining following irradiation, the photon lifetime increases, and the mode narrows.

In addition to linewidth changes, loss of Ru headgroups should alter the excess polarizability, and hence refractive index, at the resonator surface, leading to a shift in position of the resonance. Attempts to monitor uncaging through resonance shifts, however, did not reveal a clear effect compared to baseline drift during the course of exposure. As discussed elsewhere,[37] changes in resonance linewidth are more robust to baseline drift than are shifts in resonance position.

To further confirm presence of deprotected amines on the equatorial mode, resonators were reacted with the NHS ester of AF-488 and imaged by confocal fluorescence microscopy. The resultant AF-488 fluorescence localized in a band near the equator as expected, and as shown by the red arrows in Fig. 6a. The surface modification was not always uniform, however; for example, Fig. 6b shows a less successful attempt in which the band was incomplete, presumably due to challenges in achieving uniform surface coverage during initial deposition of Ru-APTES. Despite such variations, these results indicate that resonators can be successfully patterned with a 1064 nm source, in support of a two photon deprotection mechanism.

Patterning can significantly expand capabilities of single resonators by allowing different modes to be assigned specific tasks. One application that benefits from such a multimodal capability is self-referenced sensing, in which nonspecific contributions to an overall response are removed to help isolate the specific response of interest. Self-referenced operation requires comparison of signals from at least two channels: a "sensing" channel which experiences the specific response as well as any nonspecific contributions, and a "reference" channel that separately monitors just the nonspecific contributions. Nonspecific

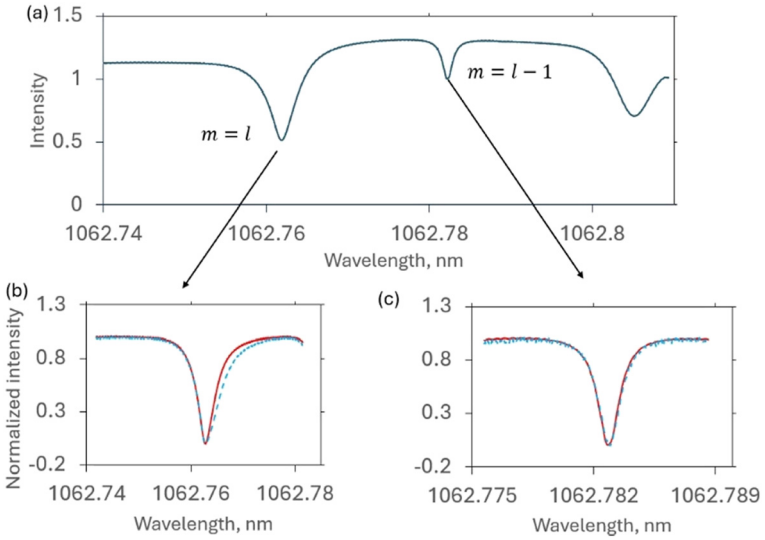

Fig. 5 Changes in linewidth after irradiation at 1064 nm. (a) Full scan showing the $m = l$ through $m = l - 2$ resonances. (b) Overlay of the equatorial $m = l$ resonance before (blue dashed trace) and after irradiation at 1064 nm (red solid trace). Q-factor: 220 000 before; 270 000 after. (c) Before and after overlay of the $m = l - 1$ resonance, which was not irradiated. Q-factor: 720 000 before; 730 000 after.

contributions could arise, for example, from drift or changes in temperature, buffer composition, or nonspecific adsorption of analyte.

In a first demonstration of WGM photopatterning to enable self-referenced sensing, the $m = l$ equatorial mode was designated as the sensing channel and, following deprotection of Ru-APTES, was modified with biotin ligands to support subsequent specific binding of avidin. The neighboring $m = l - 1$ mode served as the reference channel and was left with just Ru-APTES, without further deprotection or other functionalization. Since the separation between the $m = l$ and $m = l - 1$ regions on the resonator surface was less than 3 μm, the two channels are expected to sample nearly equivalent conditions in temperature and buffer composition, as well as nonspecific adsorption of avidin. However, only the equatorial mode should detect specific binding of avidin to biotin. Avidin binding was monitored from shifts in the resonance wavelength over the course of the assay. The self-referenced signal was calculated by subtracting the shift measured in the reference channel from that of the sensing channel. Equivalent experiments were also performed on unpatterned resonators. Unpatterned resonators had the same Ru-APTES modified surface in both the sensing ($m = l$) and reference ($m = l - 1$) channels.

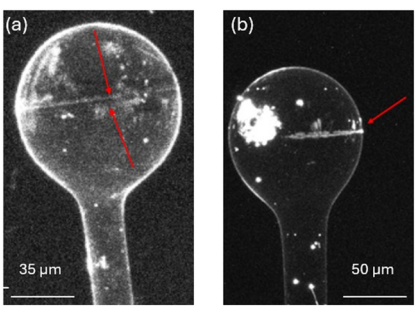

Fig. 6 Confocal fluorescence microscopy images of spheroidal resonators patterned along the $m = l$ equatorial mode (indicated by red arrows). (a) Resonator with a nearly fully patterned mode. (b) Example of an incompletely patterned mode.

For unpatterned resonators, Fig. 7a, output from the two channels (purple and red traces) was nearly identical, and dominated by pronounced nonspecific binding of avidin. Using the relation[16] $t \approx R\,(\Delta\lambda_0/\lambda_0)$ to estimate the adsorbed thickness of avidin t, the observed wavelength shift $\Delta\lambda_0$ translates to about a 3 nm layer. The blue curve shows the remnant response after self-referencing, demonstrating effective cancellation of nonspecific binding with more than 99% removal. In comparison, for resonators patterned with biotin, Fig. 7b, the sensing response exceeded that from the reference channel. Compared with the unpatterned device, this divergence is attributed to presence of specific biotin-avidin interactions on the sensing mode. The increase in coverage varied with resonator preparation, falling between 10% to 20% of the nonspecific adsorption. A level of variability between resonators was expected given variations in coupling the resonator and fiber waveguide, amplification provided by the mode, and nonuniformities in deposition of Ru-APTES (*cf.* Fig. 6).

Prior approaches to self-referenced WGM measurements were based on counterpropagating but otherwise equivalent modes whose spectral degeneracy becomes lifted by non-uniform deposition of analyte;[19,38,39] the resultant spectral separation then allows independent tracking of sensing and reference signals. In comparison with such "mode-splitting" methods, the present strategy is equally applicable to uniform and non-uniform coverages of analyte and, because

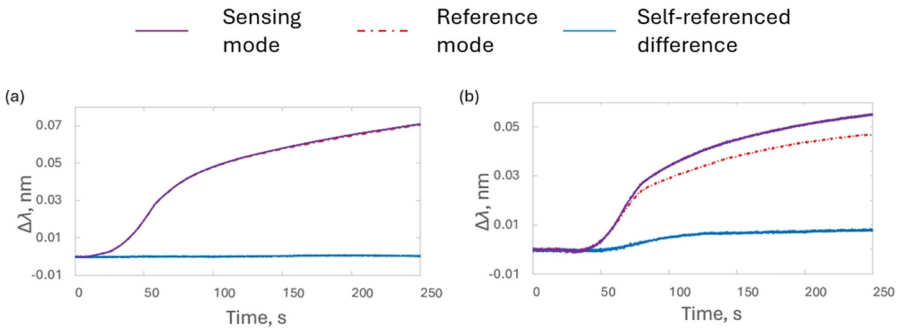

Fig. 7 Time traces of shift in resonance wavelength, $\Delta\lambda$, following injection of a 500 nM solution of avidin in 0.01 M, pH 7.3 sodium phosphate buffer. (a) Unpatterned (control) resonator. (b) Patterned resonator, with a biotin-modified sensing channel. In both plots, purple traces are the sensing signal, red curves the reference signal, and blue curves the self-referenced difference.

the modes are spectrally well separated from the outset, is also robust to linewidth broadening that can arise from absorption and tunnelling losses, especially in liquid sampling media.[40,41]

For resonators with spectrally separate modes sequential mode-by-mode patterning could also enable detection of multiple analytes on a single WGM sensor, provided the modes can be functionalized with appropriate recognition ligands. However, because intensity distributions of different modes in general overlap in space, the sequence in which modes are patterned will matter; *e.g.* spatially narrower modes may need to be patterned first, followed by wider modes to functionalize more outlying regions. For spheroidal resonators, mode-by-mode patterning could start with the equatorial mode and progress toward modes that spread farther above and below the equator. Such further optimization of the patterning process could be used to adapt single WGM sensors also to multiplexed detection.

Conclusions

Multimodal optical WGM resonators, in combination with surface patterning strategies that assign specific functionality to individual modes, open up prospects for integrating multiple sensing tasks on a single device. One strategy, presented in this report, is to directly use the resonant intensity distributions for surface patterning; the resultant patterns can then be further modified with binding ligands, antifouling compounds, or other chemistry. This approach minimizes requirements for additional hardware while ensuring alignment of the patterns for subsequent analyte assays. By utilizing several modes, a single WGM sensor can in principle be purposed for multiple tasks including detection of panels of analytes, improving specificity by targeting multiple epitopes on the same analyte, providing background correction by tracking nonspecific binding, or canceling signal offsets from variations in temperature or other environmental variables. In a self-referenced sensing approach, as demonstrated in this study, a sensing and a reference mode are used to cancel out contributions, such as from nonspecific binding, to isolate the specific response to an analyte. Self-referencing could also be used to compensate for deliberate variations in temperature or buffer composition, as commonly encountered in assays requiring tracking of binding through temperature ramps or buffer washes. By harnessing the utility of multiple modes, WGM photopatterning can significantly expand capabilities of these sensing technologies.

Data availability

All key data supporting the conclusions made in this paper have been included in the main text.

Author contributions

Y. Gao: investigation, methodology, formal analysis, writing – original draft. V. Frenkel: investigation, writing – review & editing. S. Arnold: conceptualization, supervision, writing – review & editing. R. Levicky: conceptualization, supervision, writing – original draft.

Conflicts of interest

There are no conflicts to declare.

Acknowledgements

The authors acknowledge the use of shared facilities provided through the Materials Research Science and Engineering Center (MRSEC) program of the National Science Foundation under Award Number DMR-1420073, as well as support from New York University.

References

1 Z. Nie and E. Kumacheva, *Nat. Mater.*, 2008, **7**, 277–290.
2 E. Reimhult and F. Höök, *Sensors*, 2015, **15**, 1635–1675.
3 M. Kuang, L. Wang and Y. Song, *Adv. Mater.*, 2014, **26**, 6950–6958.
4 W. Feng, E. Ueda and P. A. Levkin, *Adv. Mater.*, 2018, **30**, 1706111.

5 T. Hughes, M. Mao, A. Jones, J. Burchard, M. Marton, K. Shannon, S. Lefkowitz, M. Ziman, J. Schelter, M. Meyer, S. Kobayashi, C. Davis, H. Dai, Y. He, S. Stephaniants, G. Cavet, W. Walker, A. West, E. Coffey and P. Linsley, *Nat. Biotechnol.*, 2001, **19**, 342–347.
6 H. Li, A. Li, Z. Zhao, L. Xue, M. Li and Y. Song, *Acc. Mater. Res.*, 2021, **2**, 230–241.
7 D. J. Odde and M. J. Renn, *Trends Biotechnol.*, 1999, **17**, 385–389.
8 R. D. Piner, J. Zhu, F. Xu, S. Hong and C. A. Mirkin, *Science*, 1999, **283**, 661–663.
9 K. Salaita, Y. Wang and C. A. Mirkin, *Nat. Nanotechnol.*, 2007, **2**, 145–155.
10 J. S. Lee, R. T. Hill, A. Chilkoti and W. L. Murphy, *Biomaterials Science*, 4th edn, 2020, pp. 553–573.
11 M. Geissler and Y. Xia, *Adv. Mater.*, 2004, **16**, 1249–1269.
12 A. Kumar and G. M. Whitesides, *Appl. Phys. Lett.*, 1993, **63**, 2002–2004.
13 Y. Xia and G. M. Whitesides, *Langmuir*, 1997, **13**, 2059–2067.
14 Y. Xia and G. M. Whitesides, *Angew. Chem., Int. Ed.*, 1998, **37**, 550–575.
15 F. Vollmer, D. Braun, A. Libchaber, M. Khoshsima, I. Teraoka and S. Arnold, *Appl. Phys. Lett.*, 2002, **80**, 4057–4059.
16 F. Vollmer and S. Arnold, *Nat. Methods*, 2008, **5**, 591–596.
17 M. R. Foreman, J. D. Swaim and F. Vollmer, *Adv. Opt. Photonics*, 2015, **7**, 168–240.
18 J. Ward and O. Benson, *Laser Photonics Rev.*, 2011, **5**, 553–570.
19 J. Zhu, S. K. Ozdemir, Y.-F. Xiao, L. Li, L. He, D.-R. Chen and L. Yang, *Nat. Photonics*, 2010, **4**, 46–49.
20 J. Su, *Sensors*, 2017, **17**, 540.
21 G. C. Righini and S. Soria, *Sensors*, 2016, **16**, 905.
22 I. M. White and X. Fan, *Opt. Express*, 2008, **16**, 1020–1028.
23 S. Arnold, M. Khoshsima, I. Teraoka, S. Holler and F. Vollmer, *Opt. Lett.*, 2003, **28**, 272–274.
24 K. J. Vahala, *Nature*, 2003, **424**, 839–846.
25 A. Serpengüzel, S. Arnold, G. Griffel and J. A. Lock, *J. Opt. Soc. Am. B*, 1997, **14**, 790–795.
26 M. Iqbal, M. A. Gleeson, B. Spaugh, F. Tybor, W. G. Gunn, M. Hochberg, T. Baehr-Jones, R. C. Bailey and L. C. Gunn, *IEEE J. Sel. Top. Quantum Electron.*, 2010, **16**, 654–661.
27 G. Besselink, R. G. Heideman, E. Schreuder, L. Wevers, F. Falke and H. Vlekkert, *J. Biosens. Bioelectron.*, 2016, **7**, 1000209.
28 U. Bog, F. Brinkmann, S. Wondimu, T. Wienhold, S. Krämmer, C. Koos, H. Kalt, M. Hirtz, H. Fuchs, S. Köber and T. Mappes, *Adv. Sci.*, 2015, **2**, 1500066.
29 C. Lu, H. Nikbakht, M. Karabiyik, M. Alaydrus and I. Akca, *Opt. Express*, 2021, **29**, 42215–42224.
30 Z. Guo, Q. Lu, C. Zhu, B. Wang, Y. Zhou and X. Wu, *Opt. Express*, 2019, **27**, 12424–12435.
31 A. L. Washburn, M. S. Luchansky, A. L. Bowman and R. C. Bailey, *Anal. Chem.*, 2010, **82**, 69–72.
32 M. R. Foreman, W.-L. Jin and F. Vollmer, *Opt. Express*, 2014, **22**, 5491–5511.
33 W.-L. Jin, X. Yi, Y.-W. Hu, B.-B. Li and Y.-F. Xiao, *Appl. Opt.*, 2013, **52**, 155–161.
34 H. Ren, C.-L. Zou, J. Lu, Z. Le, Y. Qin, S. Guo and W. Hu, *J. Opt. Soc. Am. B*, 2019, **36**, 942–951.
35 Y. Hu, L. Shao, S. Arnold, Y.-C. Liu, C.-Y. Ma and Y.-F. Xiao, *Phys. Rev. A: At., Mol., Opt. Phys.*, 2014, **90**, 043847.
36 L. Shao, X.-F. Jiang, X.-C. Yu, B.-B. Li, W. R. Clements, F. Vollmer, W. Wang, Y.-F. Xiao and Q. Gong, *Adv. Mater.*, 2013, **25**, 5616–5620.
37 J. Knittel, J. D. Swaim, D. L. McAuslan, G. A. Brawley and W. P. Bowen, *Sci. Rep.*, 2013, **3**, 2974.
38 L. He, S. K. Ozdemir, J. Zhu and L. Yang, *Appl. Phys. Lett.*, 2010, **96**, 221101.
39 L. He, Ş. K. Özdemir, J. Zhu, W. Kim and L. Yang, *Nat. Nanotechnol.*, 2011, **6**, 428–432.
40 W. Kim, Ş. K. Özdemir, J. Zhu and L. Yang, *Appl. Phys. Lett.*, 2011, **98**, 141106.
41 W. Kim, Ş. K. Özdemir, J. Zhu, L. He and L. Yang, *Appl. Phys. Lett.*, 2010, **97**, 071111.
42 D. Keng, X. Tan and S. Arnold, *Appl. Phys. Lett.*, 2014, **105**, 071105.
43 R. A. Leising, S. A. Kubow, M. R. Churchill, L. A. Buttrey, J. W. Ziller and K. J. Takeuchi, *Inorg. Chem.*, 1990, **29**, 1306–1312.
44 C. A. Bessel, J. A. Margarucci, J. H. Acquaye, R. S. Rubino, J. Crandall, A. J. Jircitano and K. J. Takeuchi, *Inorg. Chem.*, 1993, **32**, 5779–5784.
45 S. Arnold, R. Ramjit, D. Keng, V. Kolchenko and I. Teraoka, *Faraday Discuss.*, 2008, **137**, 65–83.
46 G. Griffel, S. Arnold, D. Taskent, A. Serpengüzel, J. Connolly and N. Morris, *Opt. Lett.*, 1996, **21**, 695–697.
47 F. Vollmer and L. Yang, *Nanophotonics*, 2012, **1**, 267–291.
48 S. Arnold and S. Shopova, *Biophotonics: Spectroscopy, Imaging, Sensing, and Manipulation*, 2010, pp. 237–259.
49 W. Kaim, *Coord. Chem. Rev.*, 2011, **255**, 2503–2513.
50 M. Four, D. Riehl, O. Mongin, M. Blanchard-Desce, L. M. Lawson-Daku, J. Moreau, J. Chauvin, J. A. Delaire and G. Lemercier, *Phys. Chem. Chem. Phys.*, 2011, **13**, 17304–17312.
51 V. n. San Miguel, M. Álvarez, O. Filevich, R. Etchenique and A. n. del Campo, *Langmuir*, 2012, **28**, 1217–1221.
52 P. Hanczyc, B. Norden and M. Samoc, *Dalton Trans.*, 2012, **41**, 3123–3125.
53 T. Moriguchi, K. Murase and H. Sugimura, *Colloids Surf., A*, 2008, **321**, 94–98.
54 X. Deng, S. Wu, Z. Li, Y. Zhao and C. Duan, *Anal. Chem.*, 2020, **92**, 15908–15915.
55 L. M. Loftus, J. K. White, B. A. Albani, L. Kohler, J. J. Kodanko, R. P. Thummel, K. R. Dunbar and C. Turro, *Chem. – Eur. J.*, 2016, **22**, 3704–3708.
56 J. D. Knoll, B. A. Albani, C. B. Durr and C. Turro, *J. Phys. Chem. A*, 2014, **118**, 10603–10610.

57 D. Oulianov, I. Tomov, A. Dvornikov and P. Rentzepis, *Opt. Commun.*, 2001, **191**, 235–243.
58 M. Pawlicki, H. A. Collins, R. G. Denning and H. L. Anderson, *Angew. Chem., Int. Ed.*, 2009, **48**, 3244–3266.
59 Q. Zhang, X. Tian, H. Zhou, J. Wu and Y. Tian, *Materials*, 2017, **10**, 223.
60 C. Lam, P. T. Leung and K. Young, *J. Opt. Soc. Am. B*, 1992, **9**, 1585–1592.
61 M. Gorodetsky and V. Ilchenko, *Opt. Commun.*, 1994, **113**, 133–143.
62 I. Teraoka, *Appl. Opt.*, 2012, **51**, 1101–1108.
63 J. C. Swindal, D. H. Leach, R. K. Chang and K. Young, *Opt. Lett.*, 1993, **18**, 191–193.